JOURNAL OF THE AMERICAN CHEMICAL SOCIETY

Subscriber access provided by Uppsala universitetsbibliotek

Article

Boosting Interfacial Charge-Transfer Kinetics for Efficient Overall CO^2 Photoreduction via Rational Design of Coordination Spheres on Metal-Organic Frameworks

Zhi-Bin Fang, Ting-Ting Liu, Junxue Liu, Shengye Jin, Xin-Ping Wu, Xue-Qing Gong, Kecheng Wang, Qi Yin, Tian-Fu Liu, Rong Cao, and Hong-Cai Zhou

J. Am. Chem. Soc., **Just Accepted Manuscript** • DOI: 10.1021/jacs.0c05530 • Publication Date (Web): 21 Jun 2020

Downloaded from pubs.acs.org on June 21, 2020

Just Accepted

“Just Accepted” manuscripts have been peer-reviewed and accepted for publication. They are posted online prior to technical editing, formatting for publication and author proofing. The American Chemical Society provides “Just Accepted” as a service to the research community to expedite the dissemination of scientific material as soon as possible after acceptance. “Just Accepted” manuscripts appear in full in PDF format accompanied by an HTML abstract. “Just Accepted” manuscripts have been fully peer reviewed, but should not be considered the official version of record. They are citable by the Digital Object Identifier (DOI®). “Just Accepted” is an optional service offered to authors. Therefore, the “Just Accepted” Web site may not include all articles that will be published in the journal. After a manuscript is technically edited and formatted, it will be removed from the “Just Accepted” Web site and published as an ASAP article. Note that technical editing may introduce minor changes to the manuscript text and/or graphics which could affect content, and all legal disclaimers and ethical guidelines that apply to the journal pertain. ACS cannot be held responsible for errors or consequences arising from the use of information contained in these “Just Accepted” manuscripts.

is published by the American Chemical Society. 1155 Sixteenth Street N.W.,
Washington, DC 20036
Published by American Chemical Society. Copyright © American Chemical Society.
However, no copyright claim is made to original U.S. Government works, or works
produced by employees of any Commonwealth realm Crown government in the course
of their duties.

Boosting Interfacial Charge-Transfer Kinetics for Efficient Overall CO_2 Photoreduction via Rational Design of Coordination Spheres on Metal-Organic Frameworks

Zhi-Bin Fang,[†] Ting-Ting Liu,[‡] Junxue Liu,[§] Shengye Jin,[§] Xin-Ping Wu,[‡] Xue-Qing Gong,[‡] Kecheng Wang,[⊥] Qi Yin,[†] Tian-Fu Liu[†, ‖] Rong Cao,[†, ‖] * and Hong-Cai Zhou[⊥]

[†]State Key Laboratory of Structural Chemistry, Fujian Institute of Research on the Structure of Matter, Chinese Academy of Sciences, Fuzhou 350002, P. R. China

[‡] Key Laboratory for Advanced Materials, Centre for Computational Chemistry, Research Institute of Industrial Catalysis, East China University of Science and Technology, Shanghai 200237, P. R. China

[§]State Key Laboratory of Molecular Reaction Dynamics and Collaborative Innovation Center of Chemistry for Energy Materials, Dalian Institute of Chemical Physics, Chinese Academy of Sciences, Dalian 116023, P. R. China

[⊥]Department of Chemistry, Texas A&M University, College Station, Texas, 77842-3012, USA

[‖] University of Chinese Academy of Sciences, Beijing, 100049, P. R. China

KEYWORDS: Photocatalysis, Overall CO_2 Reduction, Metal-Organic Frameworks, Coordination Spheres, Charge Kinetics

ABSTRACT: The recombination of electron-hole pairs severely detracts the efficiency of photocatalysts. This issue could be addressed in metal-organic frameworks (MOFs) through optimization of the charge-transfer kinetics can be optimized via rational design of structures at atomic level. Herein, a pyrazolyl porphyrinic Ni-MOF (PCN-601), integrating light harvesters, active catalytic sites, and high surface areas all in one, has been demonstrated as a superior and durable photocatalyst for visible-light-driven overall CO_2 reduction with H_2O vapor at room temperature. Kinetic studies reveal that the robust coordination spheres of pyrazolyl groups and Ni-oxo clusters endow PCN-601 with proper energy band alignment and ultrafast ligand-to-node electron transfer. Consequently, the CO_2-to-CH_4 production rate of PCN-601 far exceeds those of the analogous MOFs based on carboxylate porphyrin and the classic Pt/CdS photocatalyst by more than 3 and 20 times respectively. Conspicuously, the reaction avoids the use of hole scavengers, and proceeds in a gaseous phase which can take full advantage of the high gas uptake of MOFs. This work demonstrates that the rational design of coordination spheres in MOF structures not only reconciles the contradiction between reactivity and stability but also greatly promotes the interfacial charge transfer to achieve optimized kinetics, providing guidance for the design of highly efficient MOF photocatalysts.

INTRODUCTION

Overall photocatalytic CO_2 reduction, mimicking the natural photosynthesis in plants, can capture and transform greenhouse CO_2 with H_2O into value-added products, which has attracted tremendous research interests in the past several years.[1-3] Besides being thermodynamic allowed for both CO_2 and H_2O half-reactions, an efficient photocatalyst for overall CO_2 photoreduction has to be superior in many kinetic aspects, such as reactants adsorption and activation, charge separation and transfer, as well as the subsequent charge utilization. Apparently, controlling these complicated kinetic properties is challenging. For traditional semiconductor-based photocatalysts, some strategies have been explored to optimize these kinetic behaviors, e.g., hetero-component incorporation,[4] facet and defect engineering,[5-6] and morphology regulation.[7-8] However, these strategies are usually restricted by tedious synthetic procedures and loss of atomic-scale control, hampering the improvements on the photocatalytic performance.

Metal-organic frameworks (MOFs), a class of porous crystalline materials demonstrating great potentials in various applications in gas storage,[9] sensing,[10] catalysis,[11] and so on, are advantageous in regard to the capability of precisely designing and tailoring structures at atomic level for functional motifs.[12-15] These features endow MOFs with the unique opportunity to orderly integrate light harvesters, catalytic sites, and high surface areas all in one and simultaneously optimize both the thermodynamics and kinetics for efficient gaseous CO_2 capture and reaction. With this notion in mind, several MOF catalysts based on photo-responsive organic ligands have been fabricated and applied for CO_2 photoreduction recently.[16-21] In these MOF catalysts, high valent metal ions (e.g. Zr^{4+}, Al^{3+}) and carboxyl groups are usually employed to achieve high stability, which, however, induce high energy barriers for reactants activation on metal nodes[22], making the ligand-to-node charge transfer energetically unfavored.[23-26] Conversely, MOFs with coordination spheres consisted of reactive metal species (e.g. Ni(II),[27] Co(II)[28] and Cu(II)[29]) and carboxyl groups are severely suffering from the structural lability even in ambient atmosphere.[30] It is clear that the photocatalytic performances of MOFs are usually limited by the contradiction between stability and reactivity. Another challenge for overall CO_2 photoreduction is the kinetically sluggish nature of the multi-electron-involved CO_2 reduction half-reaction. To unilaterally attain considerable activities for CO_2 reduction, hole scavengers or electron donors are commonly used to rapidly consume photo-generated holes in situ and supply abundant free electrons. Nevertheless, these operations are uneconomical and will confine the reactions to liquid phase rather than gaseous CO_2 atmosphere, and hence the high gas uptakes of MOFs are of no avail. Towards an overall CO_2 photoreduction in the gas phase, a boosted catalytic performance can be anticipated if one can aggregate highly active catalytic species for both half-reactions in robust coordination spheres and that permit a facile ligand-to-node charge transfer in the structure.

Herein, we have realized this hypothesis by employing a MOF (denoted as PCN-601), composed of reactive Ni-oxo cluster nodes and light-harvesting metalloporphyrin ligands connected via pyrazolyl group, as a catalyst for gas-phase overall CO_2 photoreduction with H_2O vapor at room temperature. In contrast to the carboxylate chelating groups in the conventional MOF photocatalysts, the pyrazolyl groups in our case possess a larger π-conjugation system, and cause higher π-d orbital overlaps with Ni-oxo nodes.[31] This alteration allows us to integrate catalytic active species into a robust framework, and consequently reconcile the conflict between stability and reactivity for MOF-based photocatalysts. Most importantly, such a coordination sphere dramatically accelerates the ligand-to-node electron transfer and effectively suppresses the charge recombination, offering sufficient electrons for the reduction process at the reactive Ni-oxo nodes. These features promise PCN-601 to be an efficient and durable photocatalyst for the overall CO_2 reduction. The predominant reduction product was determined to be CH_4, accomplishing the kinetically-challenging eight-electron half-reaction ($CO_2 + 8H^+ + 8e^- \rightarrow CH_4 + 2H_2O$). The oxidation product of H_2O_2 was also detected ($2H_2O + 2h^+ \rightarrow 2H^+ + H_2O_2$). To the best of our knowledge, this work is the first report on sole-MOF-executing overall CO_2 photo-reduction in gas-solid condition. Notably, the CH_4 production rate of PCN-601 far exceeds those of analogous porphyrinic MOFs and the well-known Pt/CdS system by at least 3 and 20 times, respectively. The CO_2-to-CH_4 conversions under visible light (10.1 $\mu mol \cdot h^{-1} \cdot g^{-1}$) and simulated solar irradiation (AQY = 2.18%) are among the state-of-the-art cases for room-temperature CO_2 photoreduction free from hole scavengers.

RESULT AND DISCUSSION

Synthesis and characterizations of PCN-601. PCN-601 (Figure 1a) was synthesized according to the literature[32] and the phase purity was verified by PXRD patterns (Figure 1b). The microporosity of the sample was confirmed by N_2 sorption isotherm (Figure 1c) with a BET surface area of 918.7 cm^3/g which is very close to the theoretical value (969 m^2/g) calculated by the *Zeo++* software[33]. The upturn in the high-pressure region can be ascribed to the aperture induced by the agglomeration of nanoparticles (50 ~ 100 nm as revealed in SEM image, Figure 1d). The ^1H-NMR spectra of porphyrin ligand (H_4TPP) and acid-digested MOFs were compared to confirm the metallization of Ni^{2+} in the porphyrin center. As shown in Figure 1e, the peaks at δ = -2.72 ppm (2H at porphyrin core) and δ = 13.63 ppm (4H at four pyrazole branches) presented in H_4TPP were absent in the digested PCN-601, indicating the deprotonation of porphyrin centers and pyrazole groups respectively. Thus, the target PCN-601 with Ni metalloporphyrin centers and pyrazole-NiO_x coordination spheres has been successfully constructed.

Thermodynamic feasibility for CO_2 reduction and H_2O oxidation. PCN-601 displays a wide-range visible-light absorbance

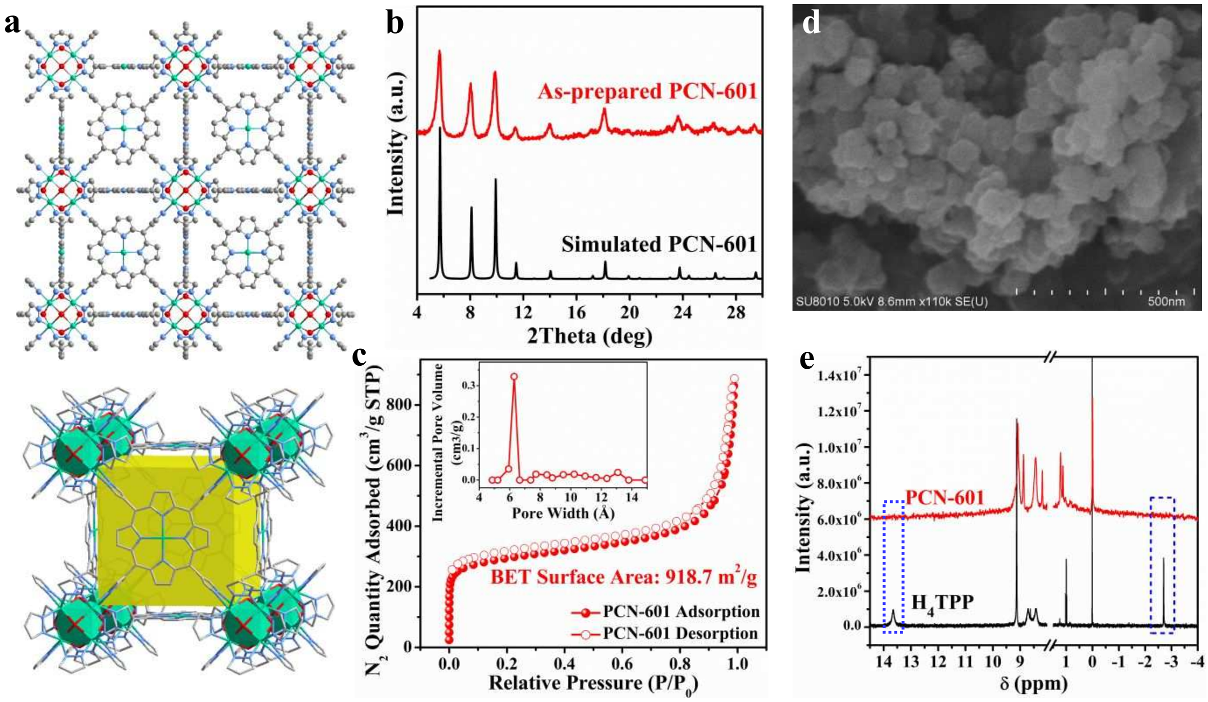

Figure 1. Construction of PCN-601: **(a)** Crystal structure (upper) and the volid volume (lower) (C, gray; O, red; N, blue; Ni, green; Void volume, yellow), **(b)** Powder X-ray diffraction (PXRD) pattern, **(c)** N_2 uptake and pore size distribution, **(d)** Scanning electron microscope (SEM) image of PCN-601; **(e)** Nuclear magnetic resonance (NMR) spectra of acid-digested PCN-601 and H_4TPP.

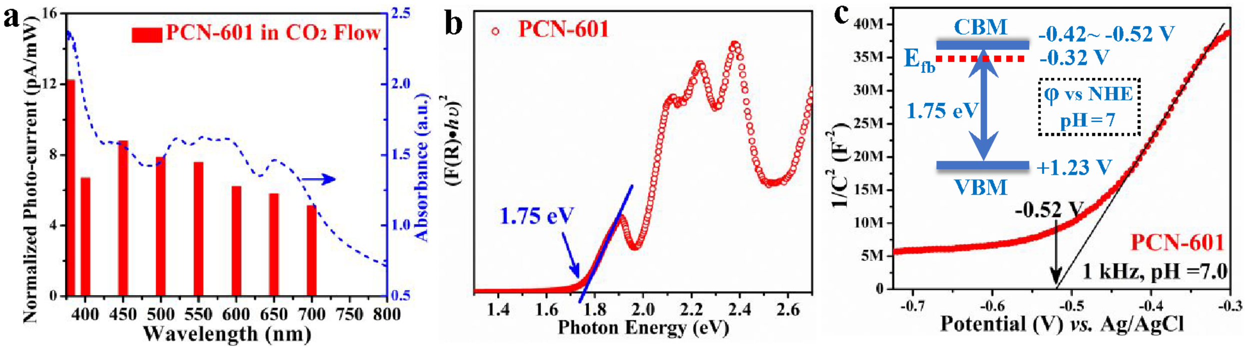

Figure 2. Illustration of the thermodynamic feasibility of PCN-601 photocatalyst: **(a)** Absorbance-dependent photon-current response of PCN-601 in gas-solid condition; **(b)** Diffuse reflectance spectra (DRS) of PCN-601 and H_4TPP via K-M transformation; **(c)** Mott-Schottky plot of the as-prepared PCN-601 electrode and calculated redox potentials.

ascribed to the light-harvesting porphyrinic macrocycle (Figure S1a). To determine the incident photon-to-current conversion, a wavelength-modulated photocurrent measurement was performed on activated PCN-601 under CO_2 flow using a gas-sensing device[34] (Figure S2, S3), which shows an apparent absorbance-dependent photocurrent as displayed in Fig 2a (Table S1), revealing the broad and effective photo-response of PCN-601. The bandgap nature was determined by fitting Tauc function to the K-M absorbance above the Urbach tail (Figure S1b).[35] As fitting to the direct-bandgap model resulted in better linearity (Figure S1c), PCN-601 can be regarded as a direct-bandgap semiconductor. Moreover, the first-principles density functional theory (DFT) calculations shows that both the valence band maximum (VBM) and the conduction band minimum (CBM) are located at the Γ point, confirming the direct-bandgap nature of PCN-601 (Figure S4). Accordingly, the bandgap value was determined to be 1.75 eV (Figure 2b), which is very close to those reported in other porphyrinic MOFs but much less than the majority of reported MOFs.[16,20,36-38] Furthermore, the conduction-band position was estimated by measuring the flat-band potential (E_{fb}) *via* Mott-Schottky plot. As shown in Figure 2c, the positive slope of the plot indicates the n-type nature of PCN-601, and E_{fb} is evaluated to be -0.52 V vs Ag/AgCl electrodes (-0.32 V vs NHE, pH = 7). Since E_{fb} of n-type semiconductors is considered to be 0.1 - 0.2 V below the CBM,[39] the CBM of PCN-601 was estimated to be -0.42 V to -0.52 V vs NHE, which is more negative than the redox potentials of CO/CO_2 (-0.48 V vs NHE, pH = 7) and CH_4/CO_2 (-0.24 V vs NHE, pH = 7). Taking the bandgap value into account, the VBM was calculated to be +1.23 V to +1.33 V vs NHE, which is more positive than the redox potential of O_2/H_2O (+0.82 V vs NHE, pH = 7). Thus, the band alignment of PCN-601 meets the thermodynamic requirements for both the half-reactions of CO_2 reduction and H_2O oxidation.

Catalytic performances in overall CO_2 photoreduction with H_2O vapor. With the high porosity, wide-range light-harvesting ligand, catalytically active metal component, as well as the proper band alignment, PCN-601 shows promises for overall CO_2 photoreduction. In a reaction of gaseous CO_2 and water vapor at room temperature, PCN-601 shows obvious wavelength-dependent photocatalytic activities (Figure S5, Table S2), which corresponds to its wide-range photon-to-current response. As shown in Figure 3a, catalyzed by PCN-601 under visible light irradiation ($\lambda \geq$ 410 nm), CO and CH_4 were steadily produced with CH_4 being of the predominant reduction product. The CO and CH_4 productions by PCN-601 considerably exceeded those obtained by the sole H_4TPP ligand (Figure 3a) as well as the Ni-metallized H_4TPP (denoted as $H_4TPP(Ni)$, Figure S6). These results highlight the vital role of the scaffold frameworks joined by pyrazolyl-NiO_x coordination spheres. Moreover, it was found that PCN-601 with fewer defects gave rise to enhanced productions of CH_4 and CO (Figure S7, Table S3). We also noticed that a trace of CO and CH_4 existed even without any catalysts present, which is probably caused by infiltrating small amount of air into the chamber during the sample handling. To identify the carbon source of the products, CO_2 was replaced by Ar gas to conduct the same experiment. As a result, both CO and CH_4 productions are equal to the blank control group, suggesting that CO and CH_4 are indeed originated from CO_2. Furthermore, the parallel isotopic $^{13}CO_2$ and D_2O labelling experiments confirmed CO_2 as the carbon source and H_2O as the proton source of produced CH_4 (Figure 3b, S8). In addition, the in-situ DRIFTS results indicated the formation of *COOH, an intermediate of CO_2-toCH_4 conversion,[40] on the surface of PCN-601 (Figure S9). Meanwhile, the main oxidation product was identified as H_2O_2 with the superoxide radical (•HO_2) being detected as the intermediate (Figure3c, S10-13).[41-43] Additionally, PCN-601 exhibited fairly reproducible activities for 5 cycle in 50 hours owing to the structural stability under the photocatalytic condition (Figure 3d, S14). Towards a straightforward comparison on the activity of PCN-601, a widely used inorganic photocatalyst of Pt-loaded CdS nanowires[44] (1%Pt/CdS, Figure S15) was also evaluated in the same reaction condition. Compared with 1%Pt/CdS, PCN-601 exhibits a slightly higher rate for CO production, but notably, a 20-fold higher rate for CH_4 production (Figure 3e).

To unveil the interplay between the structure and catalytic activity, we deliberately choose two analogous carboxylate porphyrinic MOFs, PCN-222[18] and Ni_3TCPP[45] for comparison (Figure S15c-e). PCN-601, PCN-222 and Ni_3TCPP bear the same light-harvesting porphyrin unit but differ in term of chelating groups and the resulted coordination spheres. In PCN-222, the high valent Zr-oxo metal nodes, permitting the framework robustness though (based on the Hard and Soft Acid and Base theory), does not facilitate the catalytic reaction because of its high energy barrier. Although Ni_3TCPP integrates active Ni-oxo metal nodes into the framework, it makes a severe compromise on chemical stability. Different from the carboxylate groups in the above two MOFs, the pyrazolyl groups in PCN-601 possess a larger π-conjugation system and lead to a higher degree of π-d orbital overlaps with Ni^{2+}.

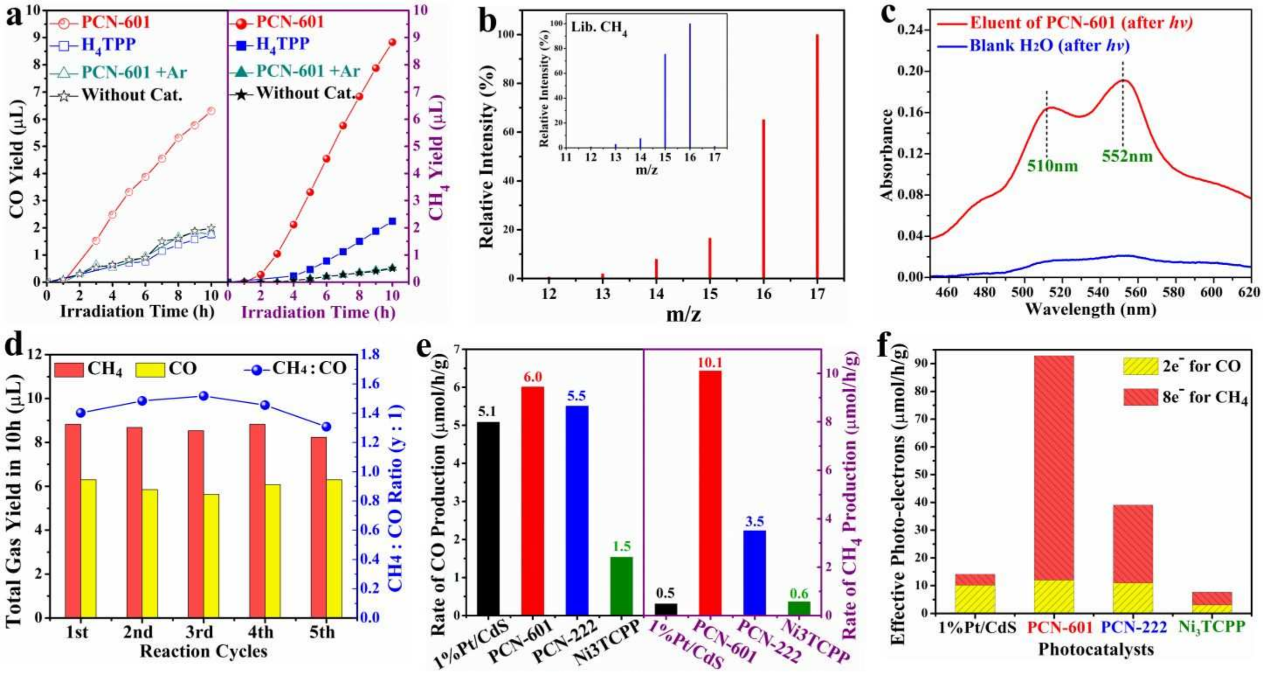

Figure 3. Photocatalytic performances of PCN-601 for CO_2 reduction: **(a)** Time-resolved CO (left) and CH_4 (right) productions; **(b)** Mass spectrum of produced $^{13}CH_4$ via isotope $^{13}CO_2$ reduction under visible light (inset: standard mass spectrum of CH_4 in data library); **(c)** Chromogenic detection of H_2O_2 after 10 hours' photocatalysis by the DPD (N, N-diethyl-1,4-phenylenediamine)/POD (horseradish peroxidase) method; **(d)** Gas yields of 5 reaction cycles (50 hours in total) and corresponding product selectivity; **(e)** Comparison of CO (left) and CH_4 (right) production rate of PCN-601 and other reported photocatalysts; **(f)** Comparison of the moles of photo-generated electrons utilized in CO_2 reduction.

These features would cause stronger coordination bonds and faster ligand-to-metal interfacial charge transfer. As a result, PCN-601 gave higher CO and CH_4 production rates than the other two MOFs (Figure 3e). Notably, the CH_4 production rate, 10.1 $\mu mol \cdot h^{-1} \cdot g^{-1}$(1.13 $\mu L \cdot h^{-1}$ per 5mg) is almost 3 times and 17 times higher than those of PCN-222 and Ni_3TCPP, respectively. To put the present work into a broader context, we also evaluated the activity of PCN-601 under simulated solar irradiation (AM 1.5G), which gave rise to a higher CH_4 production rate of 92.0 $\mu mol \cdot h^{-1} \cdot g^{-1}$ (10.3 $\mu L \cdot h^{-1}$ per 5mg, Figure S16). The apparent quantum yield (AQY) for CH_4 production under this condition was calculated to be 2.18%. To the best of our knowledge, the CO_2-to-CH_4 conversion by PCN-601 reported here is among the top records including all-inorganic photocatalyst systems without hole scavengers under either visible light or simulated solar light at room temperature (Table S4). The comparison of the moles of effective electrons in the reaction catalyzed byPCN-601, PCN-222 and Ni_3TCPP as well as 1%Pt/CdS reveals that PCN-601 utilized far more photo-generated electrons which mostly contributed to the CH_4 production (Figure 3d). After destroying the pyrazole-NiO_x connection by acid treatment, the CH_4 production rate of PCN-601 sharply drops from 10.1 $\mu mol \cdot h^{-1} \cdot g^{-1}$ to 1.5 $\mu mol \cdot h^{-1} \cdot g^{-1}$ while the CO production remains at the same level (Figure S17). This further indicate the vital role of pyrazole-NiO_x coordination sphere for CO_2 photoreduction, especially the CH_4 evolution.

Exploration of charge transfer pathways and harvesting sites. To gain a deeper insight into the charge transfer behaviors in PCN-601, the transfer pathways and harvesting sites of photo-generated electrons and holes were investigated. Electron paramagnetic resonance (EPR) spectra of the mixture of PCN-601 suspended in TEOA/acetonitrile solution (TEOA acted as hole scavenger) were collected with and without light irradiation. As shown in Figure S18, in contrast to the very weak signals detected in dark condition, visible-light irradiation induced much enhanced Ni(I) signals at $g_{\perp} = 2.05$ and $g_{/\!/} = 2.11$[46-48]. The origin of the Ni(I) signal cannot be identified by the EPR result alone, as Ni atoms exist in both the ligand and the metal node in PCN-601. Given this reason, theoretical calculations were performed to acquire more information. In the unit cell of PCN-601, the $[Ni_8(OH)_4(H_2O)_2]$ (denoted as $[Ni_8]$ nodes) coordinates with twelve porphyrin ligands via pyrazole groups in three directions (denoted as L1, L2 and L3, respectively, Figure 4a). The calculated partial density of states (PDOS) reveal that the location of the lowest unoccupied molecular orbital (LUMO) of $[Ni_8]$ node is nearly identical to that of porphyrin ligand (contributed by L3), while the highest occupied molecular orbital (HOMO) of porphyrin ligand (contributed by L1 and L2) is significantly higher than that of $[Ni_8]$ node (Figure 4b and

4c). Meanwhile, as disclosed by Figure 4c, both the ligand and $[Ni_8]$ node contribute to the lowest unoccupied crystalline orbital (LUCO) of PCN-601 and the ligand solely contributes to the highest occupied crystalline orbital (HOCO), suggesting two modes of photo-excitation may occur in PCN-601, i.e., a charge-transfer excitation (electrons of porphyrin are directly excited to the $[Ni_8]$ node) and a ligand-localized excitation. Then a time-dependent density functional theory (TD-DFT) calculation was performed to study the two possible photo-excitations using a $[Ni_8(OH)_4(H_2O)_2(HPz)_{11}H_3TPP(Ni)]$ cluster (Figure S19a) and an isolated $H_4TPP(Ni)$ ligand intercepted from PCN-601 unit cell, respectively. The results verify the presence of both modes of excitation in PCN-601 under visible light irradiation and that the ligand-localized excitations are much stronger than the direct ligand-to-node excitations (Figure S19b, Table of TD-DFT in Supporting Information-2). For the ligand-localized excitations, it is thermodynamically feasible for the photo-generated electrons to migrate from the porphyrin ligands to the $[Ni_8]$ nodes while the photo-generated holes of porphyrin are forbidden for such a ligand-to-node transfer, owing to the energy level alignment between the porphyrin ligand and the $[Ni_8]$ node discussed above (Figure 4c, middle and bottom). Hence, these results indicate that charge-separated states can be easily achieved in PCN-601. On the other hand, for PCN-222 and Ni_3TCPP, the calculated HOCO and LUCO are predominantly on the ligand (Figure S20, Table S5), indicating that the formation of charge-separated states in these two MOFs are unfavored. Furthermore, to inspect the detailed distribution of photo-excited electron in PCN-601, a constrained electronic configuration calculation[49-51] and a simulation with an added extra electron[52-53] were performed to model the behavior of photo-excited electrons. Herein, we filled the original LUCO with an extra electron in both calculations. As revealed in Figure 4d and 4e, this extra electron is localized on one Ni atom of the $[Ni_8]$ node. These results suggest that the $[Ni_8]$ node and porphyrin ligands are the electron and hole harvesting sites of PCN-601, respectively. With this information, when returning to EPR result in Figure S17, we can ascribe the origin of Ni(I) signals to the Ni-oxo nodes. Therefore, the ligand-to-node electron transfer under light irradiation in PCN-601 was revealed.

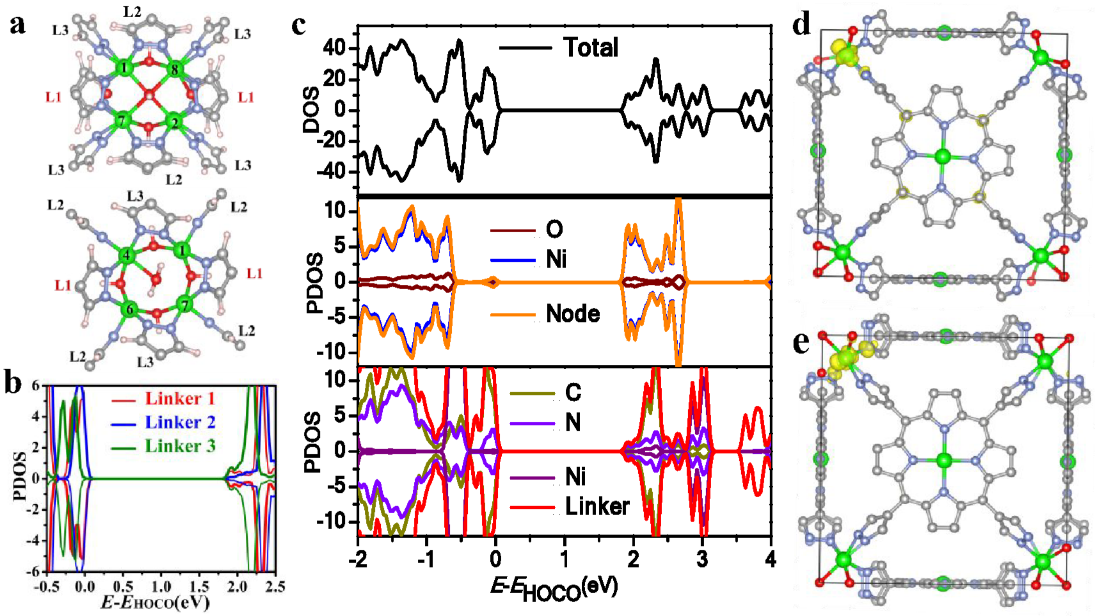

Figure 4. (a) Different views of the calculated structures of the $[Ni_8]$ cluster; **(b)** Calculated PDOS of the linkers 1, 2, and 3 of PCN-601; **(c)** Calculated DOS and PDOS for PCN-601; The most favored location of a photo-excited electron simulated by **(d)** a constrained calculation and **(e)** a calculation with an extra electron using HSE06 exchange-correlation functional (the isosurface value is 0.05 e $Å^{-3}$). HSE06 exchange-correlation functional were used for calculations of (**b-e**). For clarity, the hydrogen atoms are not shown.

Evaluation of interfacial charge separation and transfer efficacy. PCN-601 shows a π-d overlap between ligands and metal nodes (Figure S21) and shorter N-Ni bonds (2.092 Å between the pyrazole group and Ni-oxo cluster) than the O-Zr bonds (2.21 Å and 2.24 Å) in PCN-222 (Table S6), which probably provides broad and robust channels to benefit the rapid interfacial charge transfer between ligands and metal clusters. This speculation was further supported by the charge mobility evaluated via the gas-sensing currents. In an inert atmosphere without light irradiation, the current value of PCN-601 electrode is an order of magnitude higher than that of PCN-222 as shown in Figure 5a, suggesting much higher intrinsic charge mobility in PCN-601.[34] Meanwhile, the dramatically weak photoluminescence (PL) intensity of PCN-601 relative to those of PCN-222 and H_4TPP validates the efficient charge separation in PCN-601 (Figure 5b, S22, S23a). Other evidences came from the time-resolved PL decays shown in Figure S23b. The exciton lifetime of H_4TPP ligand shows only one exponential decay of $\tau = 8.99$ ns while that of PCN-601 shows two decay components with $\tau_1 < 0.24$ ns (below the detection limit of the instrument, 45.7%) and $\tau_2 = 10.01$ ns (54.3%). The τ_2 value is very close to τ value of H_4TPP, which thus is attributed to the decay manner resembling the porphyrin-localized exciton recombination in H_4TPP, while the ultrafast decay component of τ_1 indicates the existence of rapid charge separation process in PCN-601.

To gain further insight into the rapid charge separation of PCN-601, the ultrafast transient absorption (TA) spectroscopy was conducted. Under the pumping light excitation at $\lambda = 400$ nm, both porphyrin ligand and MOFs show an apparent ground-state-bleaching (GSB) signal at

~420 nm due to the state-filling effect caused by photo-generated electrons and holes (Figure 6, S24). By probing the absorption intensity at $\lambda = 418$ nm, the kinetic curves of GSB recovery were acquired. In principle, the GSB recovery corresponds to the decrease of excited states, which can be induced by either charge recombination or charge separation and transfer. For the sole $H_4TPP(Ni)$ without ligand-to-node charge transfer, the observed GSB recovery should mainly arise from the charge recombination. Figure 6a-c shows that PCN-601 with the ligand-to-node electron transfer pathway exhibits similar TA spectral features to that of the ligand but a much faster GSB recovery. To verify whether electron transfer or charge recombination play the key role to the faster GSB recovery in PCN-601, we examined the TA kinetics of $H_4TPP(Ni)$ ligand with the addition of [6,6]-phenyl-C_{61}-butyric acid methyl ester (PCBM, a well-known electron acceptor molecule) for comparison. It turns out that the addition of PCBM induced a faster GSB recovery than the sole $H_4TPP(Ni)$ system (Figure 6c, S24a). Therefore, we can attribute the accelerated GSB recovery in PCN-601 to the efficient ligand-to-node electron transfer.[54] To compare the electron transfer rates in PCN-601, PCN-222 and Ni_3TCPP, the average GSB recovery times were calculated by fitting the kinetic curves with exponential decay functions,[55] which were 72 ps for PCN-601, 215 ps for PCN-222, and 1286 ps for Ni_3TCPP, respectively (Figure 6d, Table S7). The fastest GSB recovery of PCN-601 demonstrates the most efficient ligand-to-node electron transfer among these three MOFs,[56] confirming the superiority of pyrazole-NiO_x coordination sphere than carboxyl-ZrO_x and carboxyl-NiO_x configurations (Figure 6e).

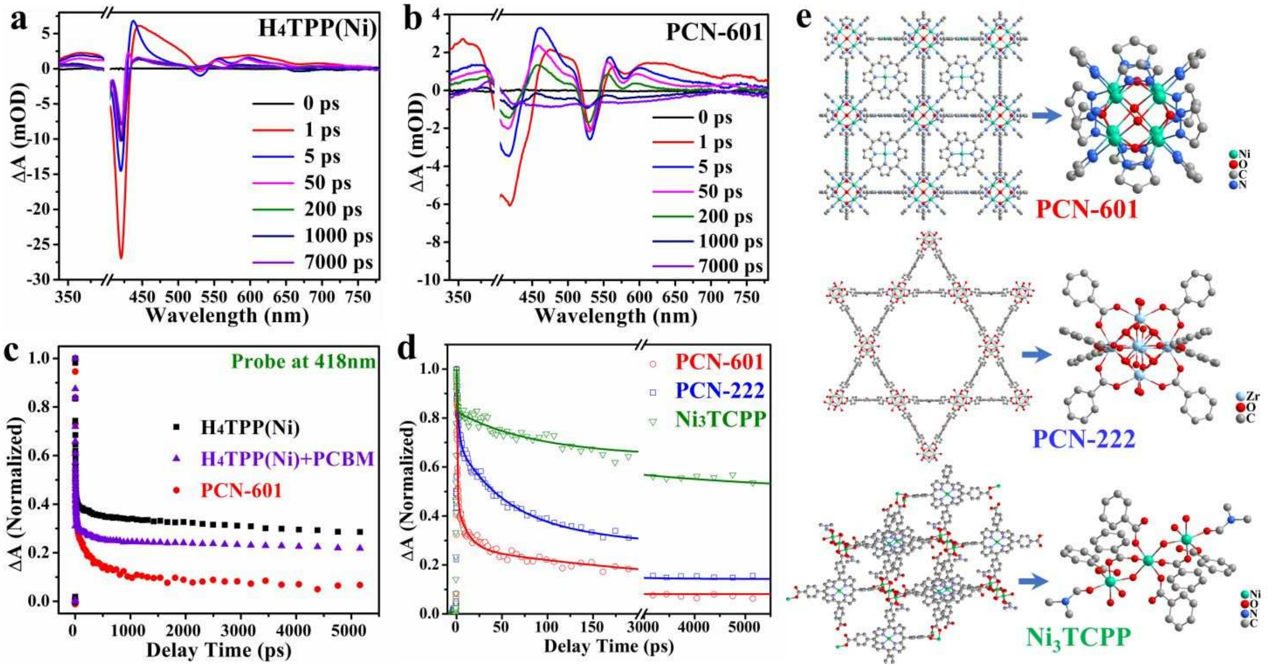

Figure 6. TA spectra of samples dispersed in DMF: **(a)** $H_4TPP(Ni)$, **(b)** PCN-601; **(c)** Corresponding normalized TA kinetic curves probed at 418 nm; **(d)** Normalized TA kinetic curves of PCN-601, PCN-222, and Ni_3TCPP (probe at $\lambda = 418$ nm); **(e)** Crystal structures and coordination spheres of PCN-601 (top), PCN-222 (middle), and Ni_3TCPP (bottom).

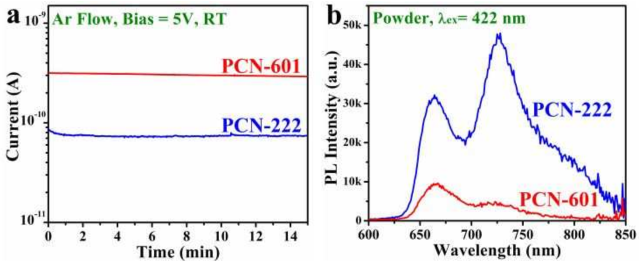

Figure 5. **(a)** Charge mobilities of PCN-601 and PCN-222 revealed by gas-sensing currents measured in Ar flow; **(b)** Solid-state PL spectra of PCN-601 and PCN-222 excited at $\lambda = 422$ nm.

The affinities and activations for reactants. The affinities between reactants and catalysts, an important aspect in kinetics especially for a heterogenous gas-solid reaction, were evaluated in PCN-601. As displayed in Figure 7a, compared with many famous sole-MOF photocatalysts (Table S6), PCN-601 exhibits a high absorption capacity (82.4 cm^3/g at 273K, 1 atm) and a moderate adsorption enthalpy (21.7 kJ/mol) for CO_2, demonstrating the desired CO_2 affinity for photocatalysis. As described above, in N_2 atmosphere, EPR spectra of PCN-601 showed characteristic Ni(I) signals ($g_{\perp} = 2.05$ and $g_{//} = 2.11$) under visible-light illumination. These signals lasted for over 20 minutes even after turning light off, suggesting that the harvested electrons were hardly delivered to N_2 (Figure 7b). However, with a substitution of N_2 for CO_2, these signals disappeared, which be explained by the fact that the electron at Ni(I) migrated to CO_2 for initial activation and then Ni(I) turn back into diamagnetic Ni(II). Meanwhile, the DFT calculations of the PCN-601 model (Figure S25) show that CO_2 molecules were preferentially adsorbed at the Ni atoms of the Ni-oxo cluster where most of the photo-excited electrons localized. And the adsorption energy (E_{ads}) was enhanced with the presence of photo-excited electron, which could benefit the activation of CO_2 (Table S8). The affinity for H_2O, the other reactant in overall

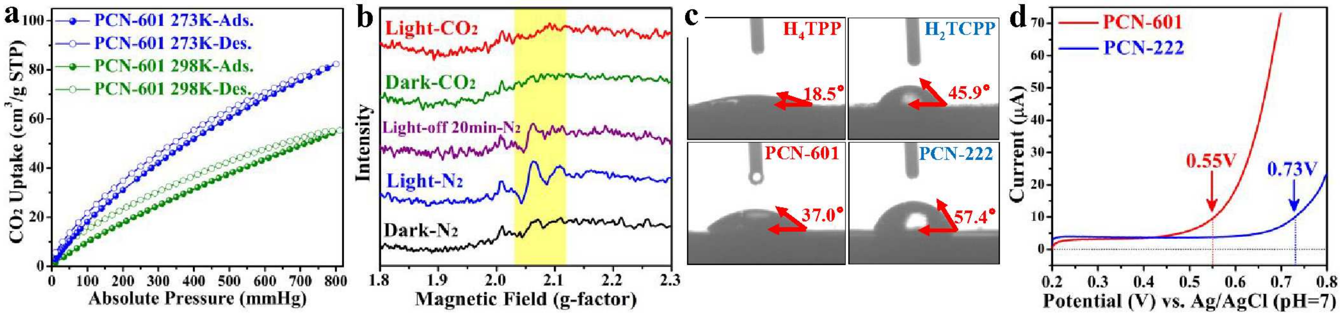

Figure 7. Reactant adsorption and activation on PCN-601: **(a)** CO_2 adsorption; **(b)** TEOA-assisted EPR spectra; **(c)** Measurement of water contact angles; (d) Electrochemical linear sweep voltammetry (LSV) curves for water oxidation.

CO_2 photoreduction, was inspected via evaluating the hydrophilicity of PCN-601. The contact-angle tests showed that H_4TPP ligand exhibits a smaller contact angle (18.5°) than H_2TCPP ligand (45.9°) (Figure 7c), implying higher hydrophilicity of pyrazolyl branches than benzoyloxy branches of ligands. With pyrazole-involved coordination spheres, PCN-601 indeed showed a higher H_2O affinity (37.0°) than PCN-222 (57.4°). In addition, PCN-601 exhibited a lower overpotential than PCN-222 for electrocatalytic water oxidation according to the LSV curves (Figure 7d). Although the condition was different with the gas-solid photocatalysis, this result could roughly estimate the capacity of H_2O activation for the two MOFs. Overall, the high affinity and facile activation ability of PCN-601 toward both H_2O and CO_2 reactants were disclosed, which could be another kinetic advantage to facilitate the photocatalytic reaction.

Based on the above investigations, we propose the mechanism of overall CO_2 photoreduction in PCN-601. The porphyrin ligand serves as the light harvester and generates electron-hole pairs. Photo-generated electrons rapidly transfer to the Ni-oxo nodes across the broad and robust N-Ni channels while the hole migration is inhibited, promoting the charge separation (Scheme 1a). Afterwards, sufficient holes accumulating on porphyrin macrocycles oxidize the absorbed H_2O molecules into H_2O_2 and generate protons. The abundant electrons harvested at Ni-oxo nodes reduce CO_2 to the *COOH intermediates, which are further reduced to CO and CH_4 (a multi-electron-involved hydrogenation process) (Scheme 1b). During the entire process, the efficient interfacial charge separation caused by the ultrafast electron transfer plays a key role in the multi-electron-involved CH_4 evolution.

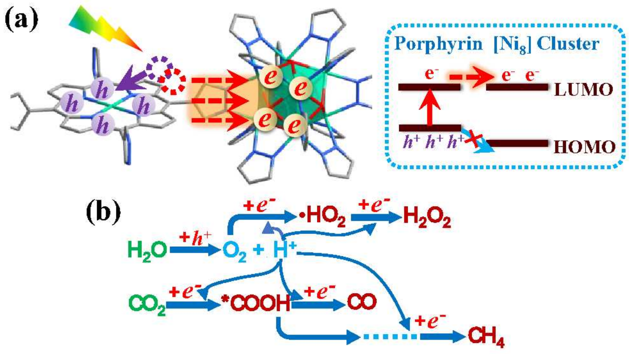

Scheme 1. Proposed mechanism for the overall CO_2 photoreduction of PCN-601: **(a)** charge separation and transfer though coordination sphere; **(b)** reaction pathways for the products.

CONCLUSIONS

In summary, we have demonstrated that PCN-601 is an advanced photocatalyst for visible-light-driven overall gas-phase CO_2 reduction in the presence of H_2O vapor. The catalytic activity and selectivity for CH_4 production of PCN-601 far exceed the analogous carboxyl porphyrinic MOFs and well-known inorganic Pt/CdS photocatalysts, which is among the top cases for overall CO_2 photoreduction. Based on comprehensive studies on kinetic mechanisms, the superior performances of PCN-601 can be attributed to the optimized coordination sphere in structure which successfully reconciles the demands of reactive metal components and robust framework, and most importantly, achieves ultrafast ligand-to-node electron migration and efficient charge separation in the photocatalyst. These findings provide insights into the structure-property relationships, which has yet to be clear for MOF photocatalysis, and are anticipated to provide significant guidance for the design of highly-efficient photocatalysts.

ASSOCIATED CONTENT

Supporting Information

The Supporting Information is available free of charge via the Internet at http://pubs.acs.org.

Experimental details for the preparations, characterizations of materials, Figure S1-25, Table S1-8, Computational details, Table of TD-DFT calculation.

AUTHOR INFORMATION

Corresponding Author

*rcao@fjirsm.ac.cn

ORCID

Zhi-Bin Fang: 0000-0003-3650-4983
Tian-Fu Liu: 0000-0001-9096-6981
Rong Cao: 0000-0002-2398-399X

Author Contributions

All authors have given approval to the final version of the manuscript.

Notes

The authors declare no competing financial interest.

ACKNOWLEDGMENT

This work was financially supported by National Natural Science Foundation of China (NSFC, Grant 21802142, 21871267, 21825301 and 21520102001), National Key R&D Program of China (Grant 2018YFA0208600), the Recruitment Program of Global Youth Experts, the CAS Strategic Priority Research Program (Grant XDB20000000) and the Key

Research Program of Frontier Science CAS (QYZDJ-SSW-SLH045).

REFERENCES

(1) Li, R.; Zhang, W.; Zhou, K. Metal-Organic-Framework-Based Catalysts for Photoreduction of CO_2. *Adv. Mater.* **2018**, *30*, 1705512.

(2) Tu, W.; Zhou, Y.; Zou, Z. Photocatalytic conversion of CO_2 into renewable hydrocarbon fuels: state-of-the-art accomplishment, challenges, and prospects. *Adv. Mater.* **2014**, *26*, 4607.

(3) Li, K.; Peng, B.; Peng, T. Recent Advances in Heterogeneous Photocatalytic CO_2 Conversion to Solar Fuels. *ACS Catal.* **2016**, *6*, 7485.

(4) Low, J.; Yu, J.; Jaroniec, M.; Wageh, S.; Al-Ghamdi, A. A. Heterojunction Photocatalysts. *Adv. Mater.* **2017**, *29*.

(5) Yu, J.; Low, J.; Xiao, W.; Zhou, P.; Jaroniec, M. Enhanced photocatalytic CO_2-reduction activity of anatase TiO_2 by coexposed {001} and {101} facets. *J. Am. Chem. Soc.* **2014**, *136*, 8839.

(6) Hoch, L. B.; Szymanski, P.; Ghuman, K. K.; He, L.; Liao, K.; Qiao, Q.; Reyes, L. M.; Zhu, Y.; El-Sayed, M. A.; Singh, C. V.; Ozin, G. A. Carrier dynamics and the role of surface defects: Designing a photocatalyst for gas-phase CO_2 reduction. *Proc. Natl. Acad. Sci.* **2016**, *113*, E8011.

(7) Liu, Q.; Zhou, Y.; Kou, J.; Chen, X.; Tian, Z.; Gao, J.; Yan, S.; Zou, Z. High-yield synthesis of ultralong and ultrathin Zn_2GeO_4 nanoribbons toward improved photocatalytic reduction of CO_2 into renewable hydrocarbon fuel. *J. Am. Chem. Soc.* **2010**, *132*, 14385.

(8) Wang, S.; Guan, B. Y.; Lu, Y.; Lou, X. W. D. Formation of Hierarchical In_2S_3-$CdIn_2S_4$ Heterostructured Nanotubes for Efficient and Stable Visible Light CO_2 Reduction. *J. Am. Chem. Soc.* **2017**, *139*, 17305.

(9) Li, J. R.; Sculley, J.; Zhou, H. C. Metal-organic frameworks for separations. *Chem. Rev.* **2012**, *112*, 869.

(10) Kreno, L. E.; Leong, K.; Farha, O. K.; Allendorf, M.; Van Duyne, R. P.; Hupp, J. T. Metal-organic framework materials as chemical sensors. *Chem. Rev.* **2012**, *112*, 1105.

(11) Lee, J.; Farha, O. K.; Roberts, J.; Scheidt, K. A.; Nguyen, S. T.; Hupp, J. T. Metal-organic framework materials as catalysts. *Chem. Soc. Rev.* **2009**, *38*, 1450.

(12) Lalonde, M.; Bury, W.; Karagiaridi, O.; Brown, Z.; Hupp, J. T.; Farha, O. K. Transmetalation: routes to metal exchange within metal–organic frameworks. *J. Mater. Chem. A* **2013**, *1*, 5453.

(13) Lan, Y. Q.; Li, S. L.; Jiang, H. L.; Xu, Q. Tailor-made metal-organic frameworks from functionalized molecular building blocks and length-adjustable organic linkers by stepwise synthesis. *Chem. Eur. J.* **2012**, *18*, 8076.

(14) Hod, I.; Sampson, M. D.; Deria, P.; Kubiak, C. P.; Farha, O. K.; Hupp, J. T. Fe-Porphyrin-Based Metal–Organic Framework Films as High-Surface Concentration, Heterogeneous Catalysts for Electrochemical Reduction of CO_2. *ACS Catal.* **2015**, *5*, 6302.

(15) Guo, G.; Yao, Y.; Wu, K.; Wu, L.; Huang, J. Studies on the Structure-Sensitive Functional Materials. *Progress In Chemistry* **2001**, *13*, 151.

(16) Fu, Y.; Sun, D.; Chen, Y.; Huang, R.; Ding, Z.; Fu, X.; Li, Z. An amine-functionalized titanium metal-organic framework photocatalyst with visible-light-induced activity for CO_2 reduction. *Angew. Chem. Int. Ed.* **2012**, *51*, 3364.

(17) Fateeva, A.; Chater, P. A.; Ireland, C. P.; Tahir, A. A.; Khimyak, Y. Z.; Wiper, P. V.; Darwent, J. R.; Rosseinsky, M. J. A water-stable porphyrin-based metal-organic framework active for visible-light photocatalysis. *Angew. Chem. Int. Ed.* **2012**, *51*, 7440.

(18) Xu, H. Q.; Hu, J.; Wang, D.; Li, Z.; Zhang, Q.; Luo, Y.; Yu, S. H.; Jiang, H. L. Visible-Light Photoreduction of CO_2 in a Metal-Organic Framework: Boosting Electron-Hole Separation via Electron Trap States. *J. Am. Chem. Soc.* **2015**, *137*, 13440.

(19) Chen, E. X.; Qiu, M.; Zhang, Y. F.; Zhu, Y. S.; Liu, L. Y.; Sun, Y. Y.; Bu, X.; Zhang, J.; Lin, Q. Acid and Base Resistant Zirconium Polyphenolate-Metalloporphyrin Scaffolds for Efficient CO_2 Photoreduction. *Adv. Mater.* **2017**, *1704388*.

(20) Sun, D.; Fu, Y.; Liu, W.; Ye, L.; Wang, D.; Yang, L.; Fu, X.; Li, Z. Studies on photocatalytic CO_2 reduction over NH_2-Uio-66(Zr) and its derivatives: towards a better understanding of photocatalysis on metal-organic frameworks. *Chem. Eur. J.* **2013**, *19*, 14279.

(21) Zhang, H.; Wei, J.; Dong, J.; Liu, G.; Shi, L.; An, P.; Zhao, G.; Kong, J.; Wang, X.; Meng, X.; Zhang, J.; Ye, J. Efficient Visible-Light-Driven Carbon Dioxide Reduction by a Single-Atom Implanted Metal-Organic Framework. *Angew. Chem. Int. Ed.* **2016**, *55*, 14310.

(22) Dickens, C. F.; Montoya, J. H.; Kulkarni, A. R.; Bajdich, M.; Nørskov, J. K. An electronic structure descriptor for oxygen reactivity at metal and metal-oxide surfaces. *Surface Science* **2019**, *681*, 122.

(23) Lee, Y.; Kim, S.; Kang, J. K.; Cohen, S. M. Photocatalytic CO_2 reduction by a mixed metal (Zr/Ti), mixed ligand metal-organic framework under visible light irradiation. *Chem. Commun.* **2015**, *51*, 5735.

(24) De Vos, A.; Hendrickx, K.; Van Der Voort, P.; Van Speybroeck, V.; Lejaeghere, K. Missing Linkers: An Alternative Pathway to UiO-66 Electronic Structure Engineering. *Chemistry of materials* **2017**, *29*, 3006.

(25) Wu, X. P.; Gagliardi, L.; Truhlar, D. G. Cerium Metal-Organic Framework for Photocatalysis. *J. Am. Chem. Soc.* **2018**, *140*, 7904.

(26) Wu, X.-P.; Gagliardi, L.; Truhlar, D. G. Metal doping in cerium metal-organic frameworks for visible-response water splitting photocatalysts. *J. Chem. Phys.* **2019**, *150*, 041701.

(27) Gong, M.; Wang, D.-Y.; Chen, C.-C.; Hwang, B.-J.; Dai, H. A mini review on nickel-based electrocatalysts for alkaline hydrogen evolution reaction. *Nano Res.* **2015**, *9*, 28.

(28) Kanan, M. W.; Surendranath, Y.; Nocera, D. G. Cobalt-phosphate oxygen-evolving compound. *Chem. Soc. Rev.* **2009**, *38*, 109.

(29) Ran, J.; Jaroniec, M.; Qiao, S. Z. Cocatalysts in Semiconductor-based Photocatalytic CO_2 Reduction:

Achievements, Challenges, and Opportunities. *Adv. Mater.* **2018**, *30*.

(30) Yuan, S.; Qin, J. S.; Lollar, C. T.; Zhou, H. C. Stable Metal-Organic Frameworks with Group 4 Metals: Current Status and Trends. *ACS Cent. Sci.* **2018**, *4*, 440.

(31) Aubrey, M. L.; Wiers, B. M.; Andrews, S. C.; Sakurai, T.; Reyes-Lillo, S. E.; Hamed, S. M.; Yu, C. J.; Darago, L. E.; Mason, J. A.; Baeg, J. O.; Grandjean, F.; Long, G. J.; Seki, S.; Neaton, J. B.; Yang, P.; Long, J. R. Electron delocalization and charge mobility as a function of reduction in a metal-organic framework. *Nat. Mater.* **2018**, *17*, 625.

(32) Wang, K.; Lv, X. L.; Feng, D.; Li, J.; Chen, S.; Sun, J.; Song, L.; Xie, Y.; Li, J. R.; Zhou, H. C. Pyrazolate-Based Porphyrinic Metal-Organic Framework with Extraordinary Base-Resistance. *J. Am. Chem. Soc.* **2016**, *138*, 914.

(33) Willems, T. F.; Rycroft, C. H.; Kazi, M.; Meza, J. C.; Haranczyk, M. Algorithms and tools for high-throughput geometry-based analysis of crystalline porous materials. *Microporous and Mesoporous Materials* **2012**, *149*, 134.

(34) Yao, M. S.; Tang, W. X.; Wang, G. E.; Nath, B.; Xu, G. MOF Thin Film-Coated Metal Oxide Nanowire Array: Significantly Improved Chemiresistor Sensor Performance. *Adv. Mater.* **2016**, *28*, 5229.

(35) Zhang, J. H.; Clark, D. J.; Brant, J. A.; Sinagra, C. W., 3rd; Kim, Y. S.; Jang, J. I.; Aitken, J. A. Infrared nonlinear optical properties of lithium-containing diamond-like semiconductors $Li_2ZnGeSe_4$ and $Li_2ZnSnSe_4$. *Dalton Trans.* **2015**, *44*, 11212.

(36) Diercks, C. S.; Liu, Y.; Cordova, K. E.; Yaghi, O. M. The role of reticular chemistry in the design of CO_2 reduction catalysts. *Nat. Mater.* **2018**, *17*, 301.

(37) Gomes Silva, C.; Luz, I.; Llabres i Xamena, F. X.; Corma, A.; Garcia, H. Water stable Zr-benzenedicarboxylate metal-organic frameworks as photocatalysts for hydrogen generation. *Chem. Eur. J.* **2010**, *16*, 11133.

(38) Dan-Hardi, M.; Serre, C.; Frot, T.; Rozes, L.; Maurin, G.; Sanchez, C.; Ferey, G. A new photoactive crystalline highly porous titanium(IV) dicarboxylate. *J. Am. Chem. Soc.* **2009**, *131*, 10857.

(39) Shi, L.; Li, P.; Zhou, W.; Wang, T.; Chang, K.; Zhang, H.; Kako, T.; Liu, G.; Ye, J. n-type boron phosphide as a highly stable, metal-free, visible-light-active photocatalyst for hydrogen evolution. *Nano Energy* **2016**, *28*, 158.

(40) Fu, J.; Jiang, K.; Qiu, X.; Yu, J.; Liu, M. Product selectivity of photocatalytic CO_2 reduction reactions. *Materials Today* **2020**, *32*, 222.

(41) Zhang, K.; Liu, J.; Wang, L.; Jin, B.; Yang, X.; Zhang, S.; Park, J. H. Near-Complete Suppression of Oxygen Evolution for Photoelectrochemical H_2O Oxidative H_2O_2 Synthesis. *J. Am. Chem. Soc.* **2020**, *142*, 8641.

(42) Bader, H.; Sturzenegger, V.; Hoigné, J. Photometric method for the determination of low concentrations of hydrogen peroxide by the peroxidase catalyzed oxidation of N,N-diethyl-p-phenylenediamine (DPD). *Water Res.* **1988**, *22*, 1109.

(43) Wang, Z.; Ma, W.; Chen, C.; Ji, H.; Zhao, J. Probing paramagnetic species in titania-based heterogeneous photocatalysis by electron spin resonance (ESR) spectroscopy—A mini review. *Chem. Eng. J.* **2011**, *170*, 353.

(44) Yang, Y.; Zhang, Y.; Fang, Z.; Zhang, L.; Zheng, Z.; Wang, Z.; Feng, W.; Weng, S.; Zhang, S.; Liu, P. Simultaneous Realization of Enhanced Photoactivity and Promoted Photostability by Multilayered MoS_2 Coating on CdS Nanowire Structure via Compact Coating Methodology. *ACS Appl. Mater. Interfaces* **2017**, *9*, 6950.

(45) Deenadayalan, M. S.; Sharma, N.; Verma, P. K.; Nagaraja, C. M. Visible-Light-Assisted Photocatalytic Reduction of Nitroaromatics by Recyclable Ni(II)-Porphyrin Metal-Organic Framework (MOF) at RT. *Inorg. Chem.* **2016**, *55*, 5320.

(46) El-Tabl, A. S.; Shakdofa, M. M. E.; El-Seidy, A. M. A. Synthesis and spectroscopic characterization of nickel(II), cobalt(II) and copper(II) complexes of dioxime ligands. *Smart Nanocomposites* **2011**, *2*, 127.

(47) Holliger, C.; Pierik, A. J.; Reijerse, E. J.; Hagen, W. R. A spectroelectrochemical study of factor F430 nickel(II/I) from methanogenic bacteria in aqueous solution. *J. Am. Chem. Soc.* **1993**, *115*, 5651.

(48) Lovecchio, F. V.; Gore, E. S.; Busch, D. H. Oxidation and reduction behavior of macrocyclic complexes of nickel. Electrochemical and electron spin resonance studies. *J. Am. Chem. Soc.* **1974**, *96*, 3109.

(49) Melander, M.; Jonsson, E. O.; Mortensen, J. J.; Vegge, T.; Garcia Lastra, J. M. Implementation of Constrained DFT for Computing Charge Transfer Rates within the Projector Augmented Wave Method. *J. Chem. Theory. Comput.* **2016**, *12*, 5367.

(50) Bender, J. A.; Raulerson, E. K.; Li, X.; Goldzak, T.; Xia, P.; Van Voorhis, T.; Tang, M. L.; Roberts, S. T. Surface States Mediate Triplet Energy Transfer in Nanocrystal-Acene Composite Systems. *J. Am. Chem. Soc.* **2018**, *140*, 7543.

(51) Canning, A.; Chaudhry, A.; Boutchko, R.; Grønbech-Jensen, N. First-principles study of luminescence in Ce-doped inorganic scintillators. *Phys. Rev. B* **2011**, *83*.

(52) He, H.; Zapol, P.; Curtiss, L. A. A Theoretical Study of CO2 Anions on Anatase (101) Surface. *J. Phys. Chem. C* **2010**, *114*, 21474.

(53) Yang, L.; Li, X.; Zhang, G.; Cui, P.; Wang, X.; Jiang, X.; Zhao, J.; Luo, Y.; Jiang, J. Combining photocatalytic hydrogen generation and capsule storage in graphene based sandwich structures. *Nat. Commun.* **2017**, *8*, 16049.

(54) Jin, S.; Tagliazucchi, M.; Son, H.-J.; Harris, R. D.; Aruda, K. O.; Weinberg, D. J.; Nepomnyashchii, A. B.; Farha, O. K.; Hupp, J. T.; Weiss, E. A. Enhancement of the Yield of Photoinduced Charge Separation in Zinc Porphyrin–Quantum Dot Complexes by a Bis(dithiocarbamate) Linkage. *J. Phys. Chem. C* **2015**, *119*, 5195.

(55) Yan, Z. H.; Du, M. H.; Liu, J.; Jin, S.; Wang, C.; Zhuang, G. L.; Kong, X. J.; Long, L. S.; Zheng, L. S. Photo-generated dinuclear $\{Eu(II)\}_2$ active sites for selective CO_2

reduction in a photosensitizing metal-organic framework. *Nat. Commun.* **2018**, *9*, 3353.
(56) Fang, X.; Shang, Q.; Wang, Y.; Jiao, L.; Yao, T.; Li, Y.; Zhang, Q.; Luo, Y.; Jiang, H. L. Single Pt Atoms Confined into a Metal-Organic Framework for Efficient Photocatalysis. *Adv. Mater.* **2018**, *30*.

Table of Contents